A COMPARISON OF THE PERFORMANCE OF CYLINDRICAL LENS REFLECTORS AND STEPPED-INDEXED CYLINDRICAL LUNEBURG LENS REFLECTORS: SIMPLER IS BETTER?

K. Lock* and S. S. Vynogradov

Department of Mathematics, Macquarie University, NSW 2109, Australia

Abstract—This paper studies the characteristics of a constant-K lens when considered as a possible substitute for a Luneburg lens in a reflector. The competitiveness of the substitute lens is investigated in its 2D analogue, by comparing the backscattering radar cross section for the range of $D/\lambda \in (0, 200)$. The performance of cylindrical reflectors with either a constant-K lens or a cylindrical Luneburg lens (approximated by a finite number of stepped-index dielectric layers) when illuminated by an electromagnetic plane wave is studied using the semi-analytic Method of Regularization. Because of similar underlying physical principles, these studies provide an insight into the 3D analogue. The radar cross section calculations of the two reflectors for incidence angles varying from normal to grazing incidence show that the cheaper-to-manufacture constant-K lens reflector is able to provide a more powerful and stable backscattering performance than the cylindrical Luneburg lens reflector, for electrical sizes in the range considered.

1. INTRODUCTION

Most investigations on lens reflectors are concerned with the *Spherical Lens Reflectors* (*SLR*) [1–10] in the form of a stepped-index *Luneburg Lens* (*LL*) with attached *perfectly electric conducting* (*PEC*) spherical cap. The stepped-index *LL* has been extensively used as a focusing device as an approximation to the ideal *LL* with continuously varying dielectric constant. The stepped-index version reveals the same performance as expected of the ideal *LL* at a frequency range limited

by some "cut-off" frequency strictly depending on the number of concentric layers. It simply means that when using the stepped-index *LL*, the widening of the frequency range for desired performance is only possible with an increased number of layers. Such an approach is not efficient as manufacturing *LL*'s with a larger number of layers is highly costly. For this reason, some recent investigations have studied a homogeneous dielectric sphere as an alternative choice to the *LL*'s. Possessing a less pronounced focusing at any selected frequency, this simple spherical lens is advantageous when it is used as a wide-band frequency lens. It was shown in [9] that, in some cases the *radar cross section* (*RCS*) spectral characteristics of the reflector attached to a homogeneous sphere are superior those of based on the *LL*.

The objective of this paper is two-fold. The first objective, similar to [9], is to study the competitiveness of the reflector based on a homogeneous dielectric cylinder compared to that based on a cylindrical *LL*. The second objective is to study the properties of the backscattering when the incidence angle varies from that value corresponding to normal incidence to that describing the grazing incidence. This part of the investigation is of strong interest for the corresponding 3D lens reflectors, because the dependence of *RCS* versus incidence angle has not previously been studied in full. The novelties of this paper are that the analysis is done with highly accurate *Method of Regularization* (*MoR*) and it offers a fresh look at the properties of these lenses in 2D analogue, in order to ascertain the competitiveness of *CLR* and *cylindrical LL reflector* (*CLLR*) at varying incident angle. The reflectors are treated as infinitely long in this paper. According to [11], a finite cylinder can be approximated as an infinitely long cylinder when its length is a lot larger than the radius of the first Fresnel zone of the receiver; i.e., $l \gg \sqrt{r\lambda}$, where l is the length of the cylinder, r is the range and λ is the wavelength.

The remainder of this paper is outlined as follows. First, we describe the geometry of the reflectors and introduce the notation used. Then in Section 3, we study the focusing effect of a constant-K lens at different values of permittivity ε_r and electrical size $D/\lambda\,(= k_0 R/\pi)$, when illuminated by normal plane wave. The computed maximum paraxial energy intensities lead us to the locations of the focal spots, which is further used for proper placement of the strip to ensure the optimal illumination by the focused electromagnetic flux. In Section 4, we compare the effectiveness of the lenses based on the constant-K lens or *LL* by studying the spectral dependence of the *RCS* in a wide frequency range extending up to the quasi-optical region ($D/\lambda \approx 200$). The computations are done using the *MoR*, and the key steps of this method are given in the Appendix. The principal benefit of the *MoR*

is its guaranteed accuracy for structures with sharp edges, secured by the semi-analytic transform described in the Appendix. Finally, we examine behaviour of the *RCS* depending on the incident angle of the incoming plane wave in Section 5. Our conclusion appear in Section 6.

2. PROBLEM DESCRIPTION

Figure 1 gives the generic geometry of an infinitely long *L*-layered cylinder with a *PEC* strip conformally placed on its surface. With appropriate choice of parameters, this multilayered cylinder can be considered as a *CLR* or *CLLR*. All the cylinders are assumed to be parallel to the *z*-axis. The whole medium is divided by the *L* interfaces of the multilayered cylinder into $L+1$ regions. The numbering system used here is such that *Region 0* denotes the scattering region external to the cylinder (free space); while *Region L* denotes the innermost dielectric loaded layer. Each of the regions is characterized by its relative permittivity and permeability (ε_i, μ_i), for $i = 1, \ldots, L$. The infinitely thin *PEC* strip is attached to the cylinder at $\rho = R_1$. We use ϕ_0 to denote the half-angular width subtended by the strip at the centre. This cylinder is illuminated by a time harmonic plane wave impinging normally on the *z*-axis, making an angle ϕ_{inc} with respect to the *x*-axis at the centre. In this paper, only the detailed analysis for the *TM*-case is given. The time dependence of $e^{-j\omega t}$, where $j = \sqrt{-1}$,
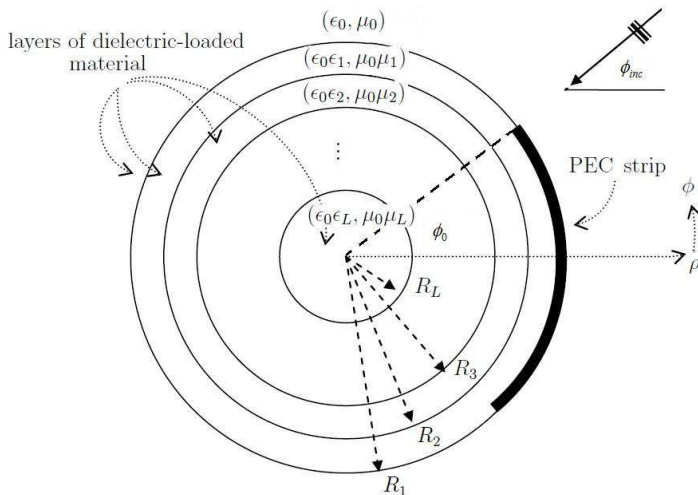

Figure 1. Cross-sectional view of a multilayered cylinder with an attached conformal *PEC* strip.

is assumed and omitted everywhere throughout the paper.

The *CLR* is a "two-layered" model of this general model, with *Region 0* and *Region 1* sharing the same physical quantities (i.e., they are both free space) while *Region 2* represents the homogeneous dielectric lens. In other words, we have a concentric layer of air surrounding the core dielectric cylinder. We use ε_r and μ_r to denote the relative physical quantities of this dielectric lens, and R denotes its radius. The *PEC* strip, which serves as a reflector, is placed at $\rho = R_1$. The location of the reflecting strip is carefully selected to lie close to the spot where incoming plane wave is focused. This is done by studying the energy distribution of the constant-K lens after the impingement of the incident plane wave.

The *LL* is a dielectric lens with its permittivity varying with the radius of the cylindrical lens. Its relative permittivity is given by the well-known formula

$$\varepsilon(\rho) = 2 - \left(\frac{\rho}{R_1}\right)^2, \quad 0 \leq \rho \leq R_1, \tag{1}$$

where R_1 is the radius of the *LL*. In this construction, the *CLLR* focuses the plane wave to a point at its surface, where the strip is located. From the manufacturing point of view, the *CLLR* is approximated by a stepped-index dielectric lens — a special case of the multilayered cylinder described where the permittivity of each layer is specified by a discretization of (1).

The scattering problem involving either a *CLR* or a *CLLR* is essentially a mixed boundary value problem at $\rho = R_1$. For reasons explained above, we employ the rigorous *MoR* instead of the more widely used numerical methods like the Method of Moments. The formulation of the problem and description are given in the Appendix.

3. FOCAL STUDIES OF A DIELECTRIC CYLINDRICAL LENS

We consider the constant-K lens of radius R excited by the E-polarized plane wave. The energy density distribution, W, resulting from the plane wave scattering is studied using the classical exact series solution. W is calculated using the following standard formula:

$$W = \frac{1}{2} \left\{ \varepsilon_0 \varepsilon_1 \left| E_z^{(1)} \right|^2 + \mu_0 \mu_1 \left| H_\phi^{(1)} \right|^2 + \mu_0 \mu_1 \left| H_\rho^{(1)} \right|^2 \right\}. \tag{2}$$

When regarded as a focusing device, the constant-K lens cylinder exhibits huge aberrations which are more pronounced for electrically large cylinders (i.e., those described by $D/\lambda \gg 1$). The ray-tracing

technique shows that paraxial rays are focused at the focus point, F, outside the cylinder, and location of the relative focus distance, f, is defined as:

$$f = \frac{OF}{OR} = \frac{\sqrt{\varepsilon_r}}{2\left(\sqrt{\varepsilon_r} - 1\right)}, \quad \text{for} \quad 1 < \varepsilon_r \leq 4 \qquad (3)$$

where O is the center of the lens. According to (3), the constant-K lens with $\varepsilon_r = 4$ collects the paraxial rays at the point $f = 1$; i.e., conditional focal point lies exactly at the surface.

Simple GO in the paraxial regime indicates that a flat or curved PEC placed exactly at the paraxial focus of the dielectric lens will produce a collimated backscattered wave from a collimated incident wave. If the PEC reflector, flat or curved, is placed away from the lens focus, then the backscattered wave becomes decollimated. In this paper, we consider the reflector to be concentric with the dielectric lens, instead of a flat screen, not only because such structure is easily adaptable to the solution method, but also because one of the goals for our study, as stated previously, is the 2D analogue study of the competitiveness of a constant-K lens reflector with varying incident angle.

However, the constant-K lens or the step-indexed cylindrical LL lens is not a perfect lens, non-paraxial rays always suffer aberration and the wavelength is not zero as for GO. The use of the term "focus point" at microwaves is somewhat tentative, since, in fact, each individual ray passing the dielectric lens crosses the optical axis at a different point inside some region called the "focal spot". The characteristic size of the focal spot is comparable with the wavelength [9]. In this section, we restrict ourselves to the calculation of the value W across the optical axis for the variation of intensity along the z-axis. The calculation of W gives us the necessary information for further insight into the energy distribution near the focal spot. More importantly, this defines the location of the maximum energy, $W_{\max}$, across the focal spot for a fixed electrical size D/λ. The dB-scaled value, $10\log_{10} W$, is plotted against the relative distance ρ/R in Figure 2.

We examine a few constant-K lenses made of material with dielectric constant from $\varepsilon_r = 2.1$ (Polytetrafluoroethylene, PTFE) to $\varepsilon_r = 3.5$ (fused quartz). According to (3), $W_{\max}$ occurs at the points $\rho/R = 1.613$ (when $\varepsilon_r = 2.1$) and $\rho/R = 1.074$ (when $\varepsilon_r = 3.5$). These values may be called the GO focal points. However, at microwaves the electrical size of a constant-K lens is always finite. When $D/\lambda = 20$, 50, 100 and 200, the calculations reveal significant discrepancies between locations of the GO focal points and the actual locations ρ/R of $W_{\max}$, for each values of D/λ. The chain of local maxima observed as discussed below is actually an interference pattern observed along
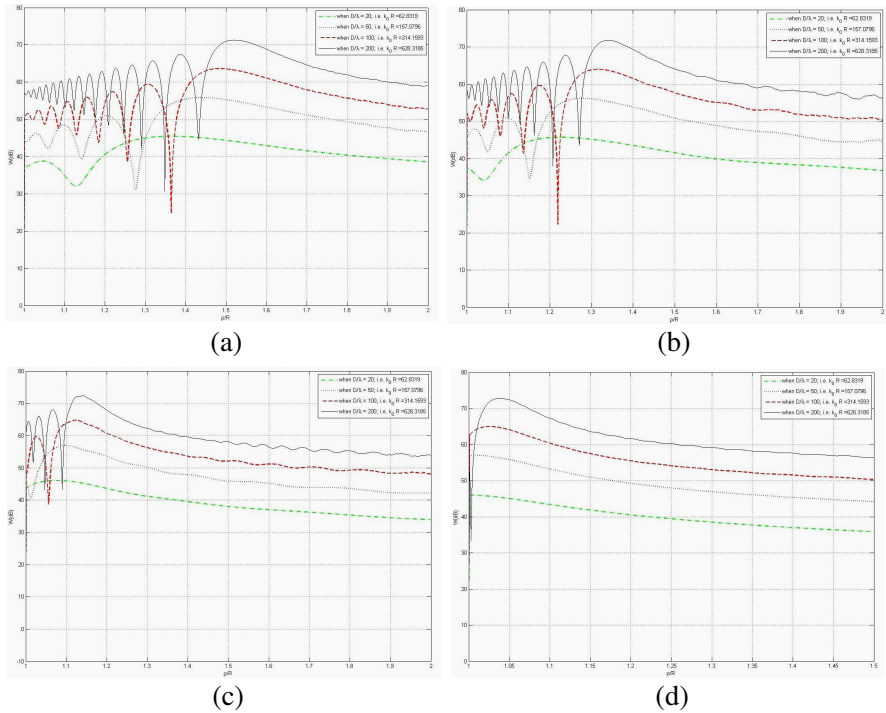
Figure 2. Distribution W across the optical axis of a constant-K lens. (a) $\varepsilon_r = 2.1$, (b) $\varepsilon_r = 2.4$, (c) $\varepsilon_r = 3.0$, and (d) $\varepsilon_r = 3.5$, where $D/\lambda = 20$ (dot-dashed, green), 50 (dotted, blue), 100 (dashed, red) and 200 (solid, black).

the axis on one side of the cusp between the caustics. For constant-K lens with $\varepsilon_r = 2.1$, these values are $\rho/R = 1.361, 1.437, 1.480,$ 1.517, respectively, as shown in Figure 2(a). Similarly, when $\varepsilon_r = 2.4$ (in Figure 2(b)), the local maxima occur, respectively, at the points $\rho/R = 1.222, 1.277, 1.318, 1.340$; when $\varepsilon_r = 3.0$ (in Figure 2(c)), the local maxima occur at the points $\rho/R = 1.081, 1.097, 1.122, 1.142,$ respectively; when $\varepsilon_r = 3.5$ (in Figure 2(d)), they correspond to the points $\rho/R = 1.001, 1.009, 1.026, 1.038$, relatively. Using formula (3), one can find that estimated GO focal points lie at the points where $(\rho/R)_{GO} = 1.613, 1.410, 1.183, 1.074$, for $\varepsilon_r = 2.1, 2.4, 3.0, 3.5,$ respectively.

It is quite evident that the local maximum approaches the focus predicted by the GO concept as the electrical size increases but aberration is visible. Nevertheless, $(\rho/R)_{\text{max paraxial } W}$ are still far away
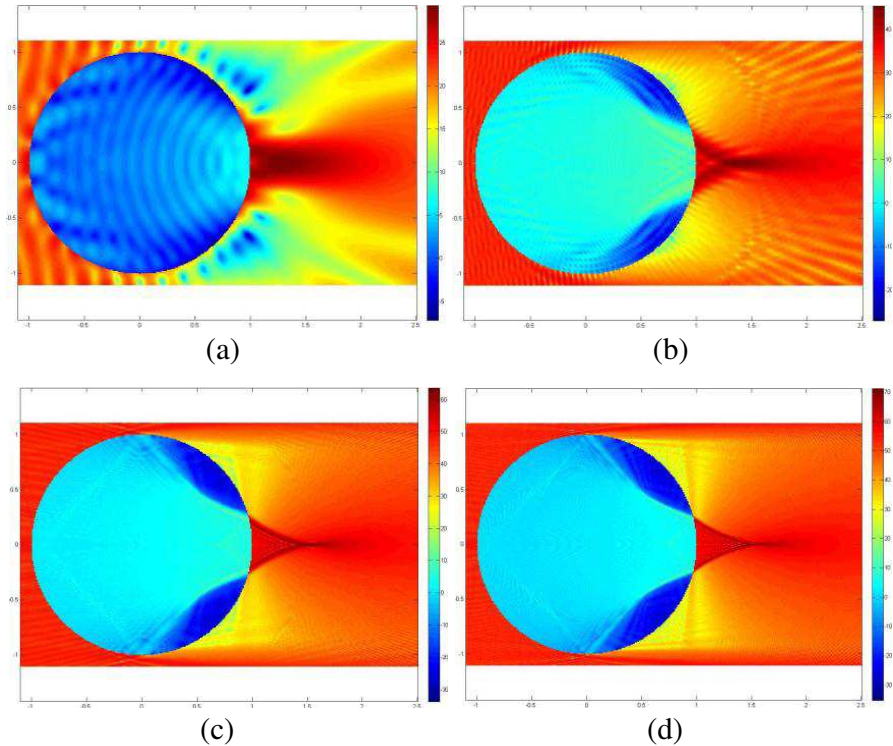
Figure 3. Spatial *EM* energy density distribution due to presence of the constant-*K* lens with $\varepsilon_r = 2.1$ and (a) $D/\lambda = 5$, (b) $D/\lambda = 20$, (c) $D/\lambda = 100$, and (d) $D/\lambda = 200$.

from $(\rho/R)_{GO}$. It is clear from Figures 3 and 4 that, instead of a single focal point as predicted by simplified *GO* concept, the actual energy distribution forms a chain of local maxima of nearly equal values at higher frequencies ($D/\lambda = 100, 200$). The ideal location of the reflector for optimal backscattering is calculated next section, taking into account the discrepancies between ideal and actual structures.

Accurate knowledge of the distribution of W across the optical axis is of paramount importance for optimal location of the *PEC* strip, in order to maximize the backscattering phenomenon. The optimal location is one of the necessary but not sufficient prerequisites forcing the radiation to be effectively reflected. The optimal choice of the angular size of the reflecting strip is equally important. The simplest idea consists in overlapping of the focused beam entirely with the strip, so that at least the *Half Power Beam Width* (*HPBW*) of the
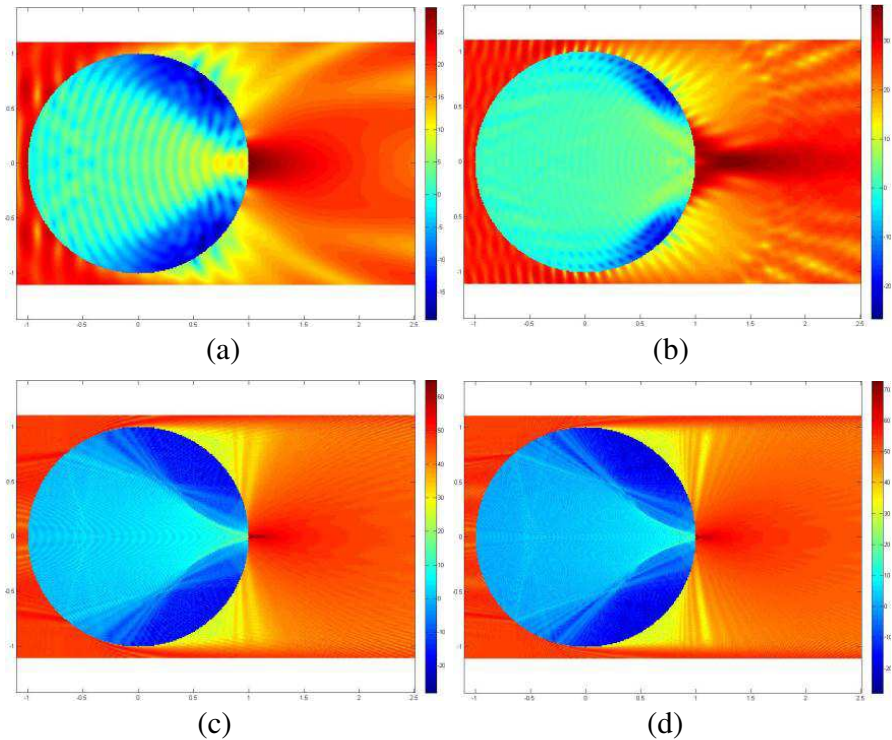
Figure 4. Spatial electromagnetic energy density distribution due to presence of the constant-K lens with $\varepsilon_r = 3.5$ and (a) $D/\lambda = 5$, (b) $D/\lambda = 20$, (c) $D/\lambda = 100$, and (d) $D/\lambda = 200$.

focused radiation would not be larger than angular size of the strip. The calculations of the spatial distribution W illustrated in Figures 3 and 4 show that it is sufficient to have cylindrical strip of the angular half-width no less than $5°$, for maximal interception of the energy in a wide range of constant-K lens with electrical size D/λ ranging from 5 up to 200.

4. CALCULATION OF BACKSCATTERING RCS

The objective of this section is to analyse the RCS behaviour of a properly designed CLR in a wide frequency range. To obtain a dimensionless measurement for studies, the backscattering RCS in dB-scale, σ_B (dB), is normalized with respect to its GO value πR and plotted against the electric size D/λ. All the computation of σ_B (dB) for both the CLR and $CLLR$ are based on solutions given by the MoR.
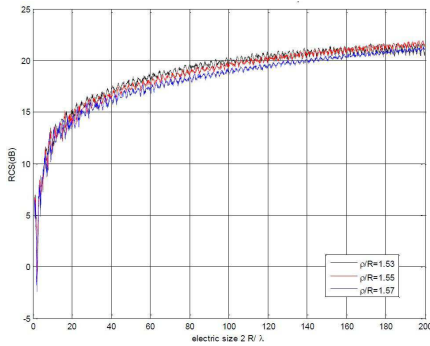
Figure 5. Spectral dependence of σ_B (dB) of a CLR ($\varepsilon_r = 2.1$) with reflector ($\phi_0 = 5°$) located at $\rho/R = 1.53$ (dotted, black), 1.55 (solid, red) and 1.57 (dot-dashed, blue), for $\phi_{inc} = 0°$.
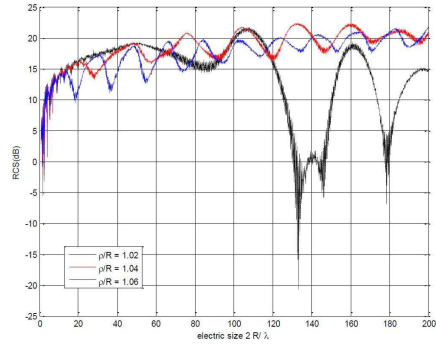
Figure 6. Spectral dependence of σ_B (dB) of a CLR ($\varepsilon_r = 3.5$) with reflector ($\phi_0 = 5°$) located at $\rho/R = 1.02$ (dotted black), 1.04 (solid red) and 1.06 (dot-dashed blue).

The values of σ_B (dB) against increasing D/λ are studied in order to locate the optimal location for the reflecting strip. The results from the study of paraxial energy density distribution, W, provide us with a good initial estimate of this optimal location. The dependence of σ_B (dB) for a CLR with reflector located in the vicinity of the focus region is computed. The computed average values of σ_B (dB) over the range $D/\lambda \in (0, 200)$ at each reflector location (ρ/R) are compared with each other. The dependences of σ_B (dB) at three locations offering the three highest average values of σ_B (dB) are displayed in Figure 5 (when $\varepsilon_r = 2.1$) and Figure 6 (when $\varepsilon_r = 3.5$). From these two figures, we deduce that the optimal locations of the reflectors are $(\rho/R)_{\max RCS} = 1.55$ ($\varepsilon_r = 2.1$) and $(\rho/R)_{\max RCS} = 1.04$ ($\varepsilon_r = 3.5$), as measured by maximal average σ_B (dB) over this band.

We can see that when the reflecting strip is located away from the optimal spot, more oscillations appear in the spectral dependence of σ_B (dB). This phenomenon is particularly obvious in Figure 6 when $\rho/R = 1.02$ (the black line). The deep null indicates the complex interference between the reflector and the constant-K lens. To better illustrate this phenomenon, the dependences of RCS for reflector located away from this optimal location are displayed in Figure 7. For practical application over a relatively wide band, the oscillation in RCS values should be as small as possible relative to the average values across the band. By this reason, behaviour as in Figure 7 is undesirable. It reinforces the reason for choosing the optimal location
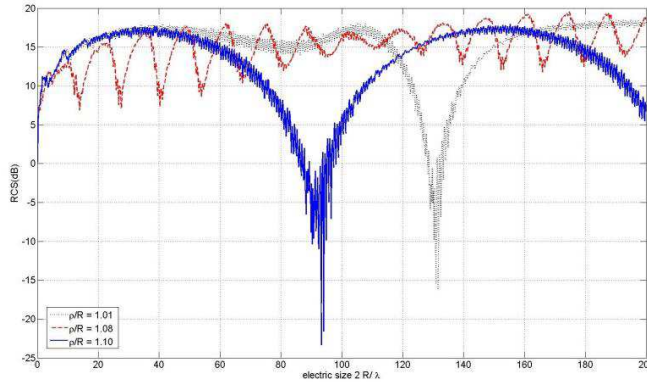
Figure 7. Spectral dependence of σ_B (dB) of a *CLR* ($\varepsilon_r = 3.5$) with reflector ($\phi_0 = 5°$) located at away from the focus region; i.e., $\rho/R = 1.01$ (dotted black), 1.08 (dashed red) and 1.10 (solid blue).

Table 1. The optimal locations of the reflector according to the three approaches, for the *CLR* with $\varepsilon_r = 2.1$, 2.4, 3.0 and 3.5. The second column displays the focus distance calculated according to the *GO* concept; the third column lists the four local maximal according to the computed paraxial energy intensity; the last column gives the location of the reflector that offers maximal average *RCS* over the range $D/\lambda \in (0, 200)$.

ε_r	$(\rho/R)_{GO}$	$(\rho/R)_{\text{max paraxial}\,W}$	$(\rho/R)_{\text{max }RCS}$
2.1	1.163	1.361, 1.437, 1.480, 1.517	1.55
2.4	1.410	1.222, 1.277, 1.318, 1.340	1.35
3.0	1.183	1.081, 1.097, 1.122, 1.142	1.15
3.5	1.074	1.001, 1.009, 1.026, 1.038	1.04

to be in the vicinity of the locations specified in the last column of Table 1, which provides the summary of the optimal locations for the strip based on the *GO* concept, the computed paraxial energy intensity and the computed maximal backscattered *RCS*, for each of the *CLR* with $\varepsilon_r = 2.1$, 2.4, 3.0 and 3.5. Therefore, to obtain the maximum backscattering for a *CLR*, when $\varepsilon_r = 2.1$, 2.4, 3.0 and 3.5, the cylindrical strip is chosen to be placed at a relative distance $(\rho/R)_{\text{max }RCS} = 1.55$, 1.35, 1.15 and 1.04, respectively.

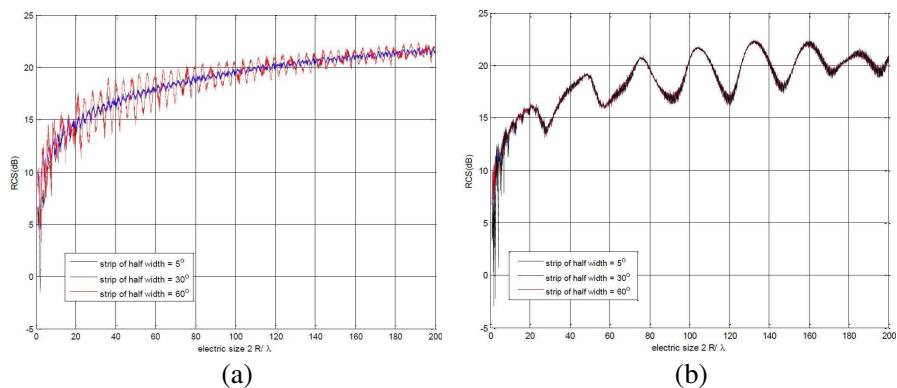In addition, observing Figure 8, we conclude that the angular

Figure 8. Effect of angular size of the cylindrical strip on the σ_B (dB) for CLR where $\phi_0 = 5°$ (dotted, black), $\phi_0 = 30°$ (dot-dashed, blue), and $\phi_0 = 60°$ (solid, red). (a) $\varepsilon_r = 2.1$, $\rho/R = 1.55$. (b) $\varepsilon_r = 3.5$, $\rho/R = 1.04$.
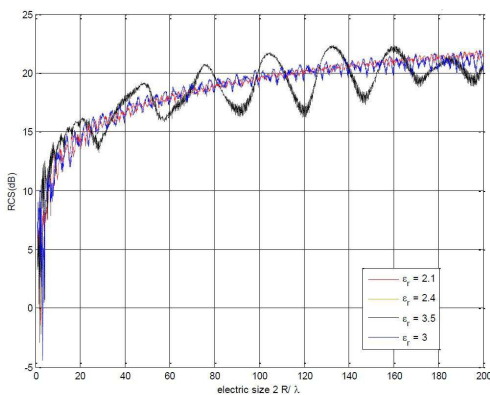

Figure 9. Spectral dependence of σ_B (dB) of CLR with $\phi_0 = 5°$ for $\varepsilon_r = 2.1$ (dashed, red), 2.4 (solid, green), 3 (dot-dashed, blue) and 3.5 (dotted, black), where $\rho/R = 1.55, 1.35, 1.15, 1.04$ respectively.

width of the PEC strip does not have significant effect on the reflectivity of the CLR. The comparative analysis of the spectral dependence for CLR in Figure 9 also shows that the performance of CLR with $\varepsilon_r = 3.5$ is marginally higher than those with $\varepsilon_r = 2.1$, 2.4 and 3.0. However, it is also worth noting that as ε_r increases, there are more oscillations in the spectral dependence of σ_B (dB). For this reason, the CLR with $\varepsilon_r = 2.1$ is preferred over those with higher ε_r.
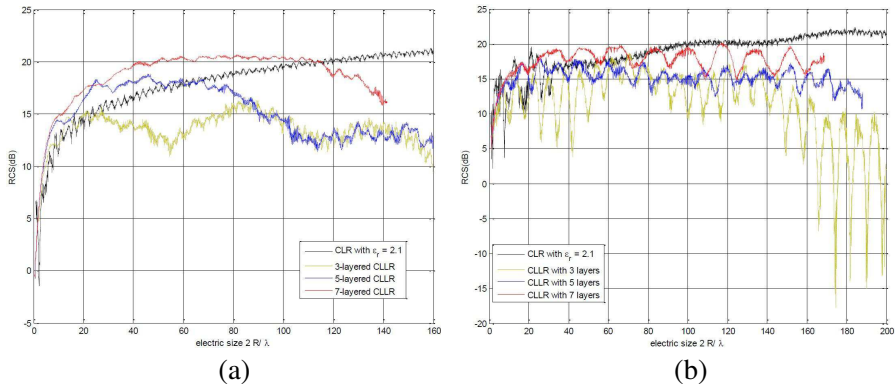
Figure 10. Spectral dependence of σ_B (dB) of CLR for $\varepsilon_r = 2.1$ (solid black), with those of $CLLR$ with 3-(dotted green), 5-(dot-dashed blue) and 7-(dashed red) layers. (a) $\phi_0 = 5°$. (b) $\phi_0 = 90°$.

Figure 10 illustrates the spectral dependence of σ_B (dB), when a plane wave is incident normally ($\phi_{inc} = 0°$) on a cylindrical reflector, and the strip is of total width 10° and 180°, respectively. They compare the performance of a CLR ($\varepsilon_r = 2.1$) with those of the L-layered $CLLR$ (constructed using stepped-index cylindrical LL). We can see from these figures that, for a minimal strip of angular size 10°, when $N = 3$, the CLR outperforms the $CLLR$ in the range $D/\lambda > 20$; when $N = 5$, the CLR outperforms the $CLLR$ in the range $D/\lambda > 60$; when $N = 7$, the CLR outperforms the $CLLR$ in the range $D/\lambda > 115$. We have even better performance from the CLR when the strip size is increased from 10° to 180°. When the strip is of total width 10°, the dependence of RCS against the electric size has an oscillatory character up to $N = 7$. As the strip size increases, more oscillations appear in the spectral dependence RCS for $CLLR$, whereas for CLR, the behaviour is still overall monotonic for both sizes of strip (10° and 180°). From our observations based on TM polarization, we draw the conclusion that the $CLLR$ can be replaced by the cheaper alternative of the CLR, which offers reasonably high and smoother spectral dependence RCS against the electric size.

5. RCS OF CLR AND $CLLR$ VERSUS INCIDENCE ANGLE ϕ_{inc}

From a general point of view, it is evident that the case of normal incidence causes the most powerful reflection, as the incident plane

wave illuminating the lens forms a focal spot right at the central part of the reflector. As has been shown previously, the strip should extend over the transverse size of a focal spot to provide strong reflection. We can observe from Figures 3 and 4 that the characteristic transverse size of a focal spot is about 1.0λ. Therefore, the geometrical size of the reflector should be no less than this value. At the incidence angle of value $\phi_{inc} = 90°$, there is no significant backscattering. This is because from the GO concept, the entire surface of a strip is completely shadowed. Thus, the effect of strong backscattering can be observed only in the range.

A simple physical argument predicts the existence of a cut-off incidence angle $\phi_{inc}^{\text{cut-off}}$ which defines the usable scanning range for the incident angle ϕ_{inc}, where $0 \leq \phi_{inc} \leq \phi_{inc}^{\text{cut-off}}$, so that a high value of RCS is practically unchanged across the angular range. It is reasonable to suppose that $\phi_{inc}^{\text{cut-off}}$ is that angle at which the right or left boundary (depending on ϕ_{inc}) of the focal spot lies exactly at the sharp edge of the reflector so that whole focal spot is covered by it. It is also clear that workable range $0 \leq \phi_{inc} \leq \phi_{inc}^{\text{cut-off}}$ strongly depends on semi-width of the reflector, ϕ_0. We assume that diffraction effects are negligible. Thus, to find the value $\phi_{inc}^{\text{cut-off}}$ we choose at the reflector surface the point at which the distance to the edge equals the angular semi-width of the focal spot; i.e., 0.5λ. Elementary algebra leads to:

$$\phi_{inc}^{\text{cut-off}} = \phi_0 - \sin^{-1}\left(\frac{\pi}{2k_0}\right). \tag{4}$$

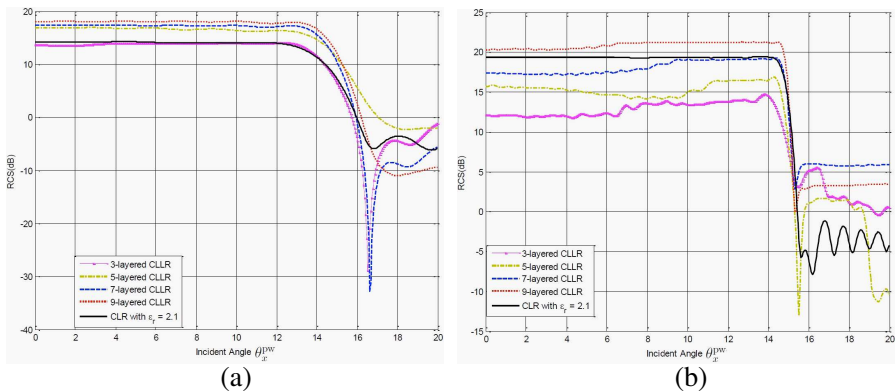According to (4), for $\phi_0 = 15°$, $k_0 R = 20\pi$, and 100π as shown

Figure 11. Comparison of σ_B (dB) against ϕ_{inc} for a CLR of $\varepsilon_r = 2.1$ (solid, black), with those of $CLLR$ with 3-(crossed-, purple), 5-(dot-dashed, green), 7-(dashed, blue) and 9-(dotted, red) layers when $\phi_0 = 15°$. (a) $k_0 R = 20\pi$. (b) $k_0 R = 100\lambda$.

(a)   (b)

Figure 12. Comparison of σ_B (dB) against ϕ_{inc} for a *CLR* of $\varepsilon_r = 2.1$ (solid, black), with those of *CLLR* with 3-(crossed-, purple), 5-(dot-dashed, green), 7-(dashed, blue) and 9-(dotted, red) layers when $\phi_0 = 90°$. (a) $k_0 R = 20\pi$. (b) $k_0 R = 100\lambda$.
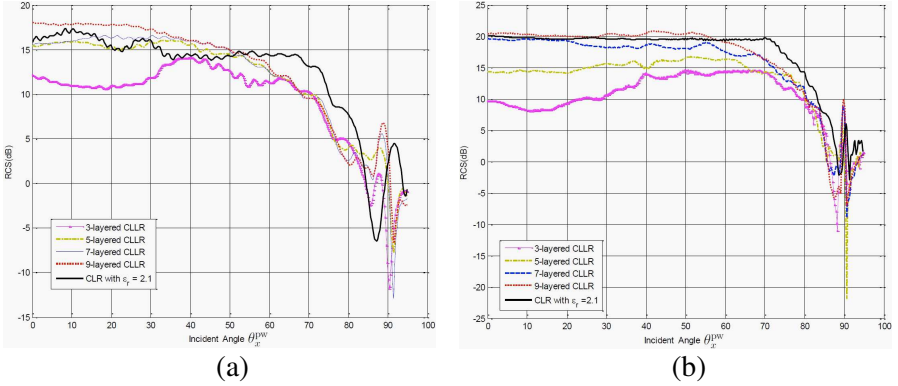
in Figure 11, we have $\phi_{inc}^{\text{cut-off}} = 13.56°$ and $\phi_{inc}^{\text{cut-off}} = 14.71°$. We can see that these results for $\phi_{inc}^{\text{cut-off}}$ are in good agreement with accurate numerical results. It should be noticed that the *CLR* provides more stable dependence of *RCS* (ϕ_{inc}) compared to the *CLLR*, even though the 5-, 7-, 9-layer *CLLR* exhibits a higher overall level of *RCS* when $k_0 R = 20\pi$ (Figure 11(a)). At higher frequency, where $k_0 R = 100\lambda$ (Figure 11(b)), the use of the *CLR* is preferable as its performance is superior to that of 3-, 5-, 7-layer *CLLR*. More strictly, our argument which led to an approximate formula for $\phi_{inc}^{\text{cut-off}}$ is reasonable only for shallow and medium size reflectors $(\phi_0 \leq 45°)$, otherwise, shielding starts to occur as well as multiple reflections.

For wider reflectors, the situation is more complicated because there are multiple reflections causing significant aberrations to the shape of the focal spot. This results in a narrowing of the range $0 \leq \phi_{inc} \leq \phi_{inc}^{\text{cut-off}}$ (as shown in Figure 12). For example, it can be seen from Figure 12(b) that, $\phi_{inc}^{\text{cut-off}}$ lies far from the angular semi-width of the reflector, $\phi_0 = 90°$. Again, as before, the scanning performance of the *CLR* is preferable to that with the *CLLR*.

6. CONCLUSION

The mixed boundary value scattering problems involving the *CLR* and *CLLR* are solved using the semi-analytic *MoR*. Accurate numerical results are computed for the *RCS* of both lens reflectors in a broad frequency band including not only the region of Rayleigh scattering

($\lambda \gg R$) and diffraction region ($\lambda \approx R$), but also the quasi-optical region ($\lambda \ll R$). The RCS characteristics of the two reflectors for incident angles varying from normal to grazing incident are also computed. From the numerical results, we deduce that CLR with lower dielectric constant ε_r are preferable to those with higher ε_r, as wavelength dependent oscillations become too strong for higher dielectric contrasts. We also observe that for higher frequencies, the scanning performance of a CLR is superior to that provided by $CLLR$, in the sense that the dependence of RCS has relatively less oscillations, and is of higher average value over the range of $D/\lambda \in (0, 200)$. The performance of the CLR is also more stable across the incident angle band. Coupled with the obvious manufacturing advantages of the simpler structure, our studies strongly suggest the simpler lens design is better.

APPENDIX A. THE METHOD OF REGULARIZATION — FROM ILL-POSED DUAL SERIES EQUATIONS TO SECOND KIND FREDHOLM MATRIX EQUATIONS

Because of the structure geometry, the electromagnetic fields are expanded in terms of cylindrical wave functions. The plane wave incident electric field can be expanded as

$$E_z^{inc}(\rho, \phi) = e^{-jk_0\rho\cos(\phi-\phi_{inc})} = \sum_{n=-\infty}^{\infty} (-j)^n J_n(k_0\rho) e^{jn(\phi-\phi_{inc})}. \quad \text{(A1)}$$

We denote the total field then in *Region i* as:

$$E_z^{(i)} = \sum_{n=-\infty}^{\infty} \left[a_n^{(i)} H_n(k_i\rho) + b_n^{(i)} J_n(k_i\rho) \right] e^{jn\phi}. \quad \text{(A2)}$$

In this formulation, notations $a_n^{(i)}$ and $b_n^{(i)}$ stand for unknown scattering coefficients to be determined. Due to the Meixner condition and the Sommerfeld radiation condition, we have $b_n^{(0)} = (-j)^n e^{-jn\phi_{inc}}$ and $a_n^{(L)} = 0$. We are thus left with $2L$ unknown coefficients to be found.

Imposing the continuity of the tangential electric field components on each of the interfaces $\rho = R_1, R_2, \ldots, R_L$, we are left with the only unknown coefficient $b_n^{(1)}$ to be solved from the mixed boundary conditions on $\rho = R_1$. The remaining coefficients can be found once $b_n^{(1)}$ is computed, using the following relations:

$$b_n^{(i-1)} = \frac{1}{1-\alpha_n^{(i)}} \left(a_n^{(i-1)} \frac{H_n(k_{i-1}R_i)}{J_n(k_iR_i)} + b_n^{(i-1)} \frac{J_n(k_{i-1}R_i)}{J_n(k_iR_i)} \right), \quad \text{(A3)}$$

$$\alpha_n^{(i-1)} = \cfrac{\frac{k_{i-1}}{\mu_{i-1}}\frac{J'_n(k_{i-1}R_i)}{J_n(k_{i-1}R_i)}\left(1 - \alpha_n^{(i)}\right) - \frac{k_i}{\mu_i}\left(\frac{J'_n(k_iR_i)}{J_n(k_iR_i)} - \alpha_n^{(i)}\frac{H'_n(k_iR_i)}{H_n(k_iR_i)}\right)}{\frac{k_{i-1}}{\mu_{i-1}}\frac{H'_n(k_{i-1}R_i)}{H_n(k_{i-1}R_i)}\left(1 - \alpha_n^{(i)}\right) - \frac{k_i}{\mu_i}\left(\frac{J'_n(k_iR_i)}{J_n(k_iR_i)} - \alpha_n^{(i)}\frac{H'_n(k_iR_i)}{H_n(k_iR_i)}\right)}$$

$$\times \frac{J_n\left(k_{i-1}R_i\right)}{J_n\left(k_{i-1}R_{i-1}\right)}\frac{H_n\left(k_{i-1}R_{i-1}\right)}{H_n\left(k_{i-1}R_i\right)}, \tag{A4}$$

$$a_n^{(i-1)} = -b_n^{(i-1)} \cdot \alpha_n^{(i-1)} \cdot \frac{J_n\left(k_{i-1}R_{i-1}\right)}{H_n\left(k_{i-1}R_{i-1}\right)}, \tag{A5}$$

$$a_n^{(0)} = b_n^{(1)}\left(1 - \alpha_n^{(1)}\right) \cdot \frac{J_n\left(k_1R_1\right)}{H_n\left(k_0R_1\right)} - \frac{Z_n\left(k_0R_1\right)}{H_n\left(k_0R_1\right)}, \tag{A6}$$

for $i = L, L-1, \ldots, 2$ in descending order, with the starting value $\alpha_n^{(L)} = 0$. Here, the primes denote differentiation of the function with respect to its argument.

As the tangential magnetic field is continuous across the dielectric surface and the tangential electric field vanishes on the *PEC* strip, a set of *dual series equations* (*DSE*) is derived from this set of mixed boundary conditions:

$$\sum_{n=-\infty}^{\infty} c_n \cdot \left(1 - \alpha_n^{(1)}\right) e^{jn\phi} = 0, \quad \forall\,|\phi| < \phi_0 \tag{A7}$$

$$\sum_{n=-\infty}^{\infty} (c_n\xi_n - d_n^*)e^{jn\phi} = 0, \quad \forall\,|\phi| > \phi_0 \tag{A8}$$

where $c_n = b_nJ_n(k_1R_1)$, $d_n^* = \frac{k_0}{\mu_0}(-j)^n e^{-jn\phi_{inc}}(J_n(k_0R_1) \cdot \frac{H'_n(k_0R_1)}{H_n(k_0R_1)} - J'_n(k_0R_1))$ and $\xi_n = \frac{k_0}{\mu_0}\frac{H'_n(k_0R_1)}{H_n(k_0R_1)}(1 - \alpha_n^{(1)}) - \frac{k_1}{\mu_1}(\frac{J'_n(k_1R_1)}{J_n(k_1R_1)} - \frac{H'_n(k_1R_1)}{H_n(k_1R_1)}\alpha_n^{(1)})$. Due to the behaviours of $J_n(z)$ and $H_n(z)$, when $n \gg z$, we introduce the following asymptotically small parameter:

$$r_n = 1 + \frac{R_1\mu_0\mu_1}{|n|\left(\mu_0 + \mu_1\right)} \times \xi_n. \tag{A9}$$

We can show that r_n and $\alpha_n^{(1)}$ have the magnitude of order $O((\frac{R_2}{R_1})^{2n}) + O(\frac{k_1R_1}{n^2})$ and $O((\frac{R_2}{R_1})^{2n})$ as $n \to \infty$. Upon substitution of r_n, the *DSE* are converted to the following set

$$Ac_0 + \sum_{n\neq 0} c_n\left(1 - \alpha_n^{(1)}\right)e^{jn\phi} = 0, \quad \forall\,|\phi| < \phi_0 \tag{A10}$$

$$Bc_0 + d_0 + \sum_{n\neq 0}(|n|\,c_n\left(1 - r_n\right) + d_n)e^{jn\phi} = 0, \quad \forall\,|\phi| > \phi_0 \tag{A11}$$

where the constants introduced are $A = -\frac{R_1\mu_0\mu_1}{\mu_0+\mu_1}(1 - \alpha_0^{(1)})$ and $B = -\frac{R_1\mu_0\mu_1}{\mu_0+\mu_1}\xi_0$, and the rescaled parameter is $d_n = \frac{R_1\mu_0\mu_1}{\mu_0+\mu_1}d_n^*$.

Meixner's condition is required to ensure that the power contained in any finite volume V is bounded. It is stated as

$$\int_V \left(\frac{1}{2}\varepsilon_0 |E|^2 + \frac{1}{2}\mu_0 |H|^2\right) dV < \infty. \qquad (A12)$$

By substituting the field expressions given in (6) and $c_n = b_n J_n(k_1 R_1)$ into (A12), Meixner's condition leads to the correct choice of the solution class for the field, which in turn provides the correct order of singularity of the fields in the vicinity of sharp edges; i.e., $\sum_n n|c_n|^2 < \infty$.

We can see that, as $n \to \infty$, the general terms of series in (A10) and (A11) decay at rates $O(n^{-3/2})$ and $O(n^{-1/2})$, respectively. In the key step of the regularization process, the slower converging series (A11) is subjected to an integration operation to equilibrate the rates of convergence of the *DSE*. The solution class, $\sum_n n|c_n|^2 < \infty$, provides sufficient condition for the justification for the termwise integration operations, as (A11) is Abel-summable.

The first step of the *MoR* involves rewriting the *DSE* in terms of Jacobi polynomials. By rescaling and levelling the convergence rates of them, the *DSE* are then transformed into two independent sets of Abel integral equations. The core of the method employs Abel inversion formulas to obtain two decoupled infinite systems of linear algebraic equations (*ISLAE*) of the second kind Fredholm. The *ISLAE* are solved by the truncation method and numerical matrix inversion. Due to the limit of space, readers are referred to [12, 13] for more detailed description of the *MoR*. The two *ISLAE* obtained have the following matrix form:

$$(I + H_i)\,\vec{x}_i = \vec{b}_i, \quad \text{for} \quad i = 1, 2 \qquad (A13)$$

where $\vec{x}_1 = \{\sqrt{n}(c_n + c_{-n})\}_{n=1}^\infty$, $\vec{x}_2 = \{\sqrt{n}(c_n - c_{-n})\}_{n=1}^\infty$ are vectors containing the unknown, I is the identity matrix operator on the Hilbert space ℓ_2 and the right hand vector components are:

$$\left[\vec{b}_1\right]_m = -\frac{\sqrt{2}Ad_0\,(1 + z_0)}{B\ln\left(\frac{1-z_0}{2}\right) - A}\frac{\widehat{P}_{m-1}^{(0,1)}(z_0)}{m} - \frac{(d_m + d_{-m})}{\sqrt{m}}$$
$$+ \sum_{n=1}^\infty \frac{(d_n + d_{-n})}{\sqrt{n}}\widehat{R}_{m-1,n-1}(z_0), \qquad (A14)$$

$$\left[\vec{b}_2\right]_m = -\frac{(d_m - d_{-m})}{\sqrt{m}} + \sum_{n=1}^{\infty} \frac{(d_n - d_{-n})}{\sqrt{n}} \widehat{Q}_{m-1,n-1}^{(0,1)}(z_0). \quad \text{(A15)}$$

Here, $z_0 = \cos\phi_0$, $\widehat{P}_n^{(\alpha,\beta)}(z_0)$ is the normalized Jacobi polynomials and $\widehat{Q}_{m,n}^{(\alpha,\beta)}(z_0)$ is the incomplete scalar product of the corresponding normalized Jacobi polynomials. We also introduce matrix operators H_1 and H_2 to denote the compact part of each *ISLAE*:

$$H_i = -\text{diag}\,(r_n) + A_i \left[\text{diag}\,(r_n) - \text{diag}\left(\alpha_n^{(1)}\right)\right], \quad \text{for} \quad i = 1,2 \quad \text{(A16)}$$

where the bounded part of each matrix operator is denoted as

$$\{A_1\}_{m,n} = \widehat{R}_{m-1,n-1}(z_0) = \widehat{Q}_{m-1,n-1}^{(1,0)}(z_0)$$
$$- \frac{B\,(1+z_0)^2}{B\,\ln\left(\frac{1-z_0}{2}\right) - A} \frac{\widehat{P}_{m-1}^{(0,1)}(z_0)}{m} \frac{\widehat{P}_{n-1}^{(0,1)}(z_0)}{n}, \quad \text{(A17)}$$

$$\{A_2\}_{m,n} = \widehat{Q}_{m-1,n-1}^{(0,1)}(z_0). \quad \text{(A18)}$$

As r_n, $\alpha_n^{(1)} \to 0$, as $n \to \infty$, the diagonal matrices involving them are compact in ℓ_2. In addition, A_1 and A_2 can be shown to be bounded, using the identity $\widehat{Q}_{n,m}^{(\alpha,\beta)}(x) = \sum_{k=0}^{\infty} \widehat{Q}_{n,k}^{(\alpha,\beta)}(x)\,\widehat{Q}_{k,m}^{(\alpha,\beta)}(x)$. In fact, A_2 is idempotent and hence, a projection operator having norm at most 1. Consequently, both the matrix operators $(I + H_1)$ and $(I + H_2)$ are Fredholm with index zero. As a result, the Fredholm alternative theorem implies the solution existence and stability of the scattering problem considered. The accuracy of the solution computed can be controlled by altering the truncation number N_{tr} of the *ISLAE*. The most notable feature of this approach and crucial for the accuracy of our calculations is that the solution computed converges not only theoretically, but also numerically to the exact solution of the *ISLAE*, as $N_{tr} \to \infty$. Good results are obtained when $N_{tr} > [k_1 R_1] + 50$.

REFERENCES

1. Hyge, G., "Studies of the focal region of a spherical reflector: Stationary phase evaluation," *IEEE Trans. Antennas and Propag.*, Vol. 16, 646–656, 1968.

2. Spencer, R. K. and G. Hyge, "Studies of the focal region of a spherical reflector. Part I: Geometric optics," *IEEE Trans. Antennas and Propag.*, Vol. 16, 317–324, 1968.

3. Spencer, R. K. and G. Hyge, "Studies of the focal region of a spherical reflector. Part II: Polarization effects," *IEEE Trans. Antennas and Propag.*, Vol. 16, 399–404, 1968.

4. Mieras, H., "Radiation pattern computation of a spherical lens using Mie series," *IEEE Trans. Antennas and Propag.*, Vol. 30, 1221–1224, 1982.

5. Ji, Y. and K. Hongo, "Field in the focal region of a dielectric spherical lens," *J. Opt. Soc. Am. A*, Vol. 8, 1721–1728, 1991.

6. Sanford, J. R., "Analysis of spherical radar cross-section enhancers," *IEEE Trans. Microwave Theory Tech.*, Vol. 43, No. 6, 1400–1403, 1995.

7. Sakurai, H., T. Hashidate, M. Ohki, K. Motojima, and S. Kozaki, "Electromagnetic scattering by the Luneberg lens with reflecting cap," *IEEE Trans. on Electromagnetic Compatibility*, Vol. 40, 94–96, 1998.

8. Vinogradov, S. S., "Microwave spherical focusing systems," *6th International Conference on Antenna Theory* & *Techniques*, 15–19, 2007.

9. Vinogradov, S. S., P. D. Smith, J. S. Kot, and N. Nikolic, "Radar cross-section studies of spherical lens reflectors," *Progress In Electromagnetics Research*, Vol. 72, 325–337, 2007.

10. Huang, M., S. Yang, W. Xiong, and Z.-P. Nie, "Design and optimization of spherical lens antennas including practical feed models," *Progress In Electromagnetics Research*, Vol. 120, 355–370, 2011.

11. Andreeva, I. B. and V. G. Samovol'kin, "Sound scattering by elastic cylinders of finite length," *Sov. Phys. Acoust.*, Vol. 22, No. 5, 361–364, 1977.

12. Vinogradov, S. S., P. D. Smith, and E. D. Vinogradova, *Canonical Problems in Scattering and Potential Theory. Part I, Chapman & Hall/CRC Monographs and Surveys in Pure and Applied Mathematics*, Vol. 122, 2001.

13. Vinogradov, S. S., P. D. Smith, and E. D. Vinogradova, *Canonical Problems in Scattering and Potential Theory. Part II, Chapman & Hall/CRC Monographs and Surveys in Pure and Applied Mathematics*, Vol. 127, 2002.